High Spatial Resolution 3D Fluid Velocimetry by Tomographic Particle Flow Velocimetry

Keishi Kumashiro*, Adam M. Steinberg†, and Masayuki Yano‡
University of Toronto, Toronto, Ontario, M3H 5T6, Canada

We introduce a tomographic, particle-based velocimetry method termed tomographic particle flow velocimetry (T-PFV). Like tomographic particle image velocimetry (T-PIV), T-PFV operates on tomographically reconstructed 3D Mie-scattering data of tracer-particle fields. However, instead of inferring the velocity field by cross-correlation, T-PFV is based on a physics-constrained motion estimation framework that is inspired by optical flow estimation. The motion constraint equation used in the present formulation of T-PFV has the same form as the linearized intensity conservation equation that is commonly used in optical flow estimation. However, instead of relying on regularized global variational schemes to address the aperture problem, T-PFV achieves closure by applying physical constraints. At present, T-PFV is formulated in terms of divergence-free radial basis functions and, thus, is suited to constant-density flows. In addition, we present a demonstration of the current formulation of T-PFV using the Johns Hopkins forced-isotropic DNS data as the ground truth, and compare to an idealized implementation of T-PIV. The results suggest that T-PFV affords a twofold improvement in spatial resolution and a 12% decrease in the relative error as compared to T-PIV.

Nomenclature

a	=	image plane area
c	=	construction point index
D	=	number of spatial dimensions (for tomographic particle flow velocimetry, $D = 3$)
$\mathbf{d}(\mathbf{x})$	=	intensity field displacement
$\tilde{\mathbf{d}}(\tilde{\mathbf{x}})$	=	optical flow displacment field
e	=	error of estimated field relative to DNS field
I	=	tomographically reconstructed 3D Mie-scattering intensity field
$\tilde{I}$	=	planar image intensity field
$\mathcal{I}_D$	=	$D \times D$ identity matrix
$K(\cdot, \mathbf{y}^c)$	=	physics-informed matrix-valued radial basis function ($D \times D$ matrix)
ℓ	=	voxel index
$\mathbf{r}$	=	coordinate relative to the center of a radial basis function
t	=	time
Δt	=	discrete time interval
$N_\mathrm{p},\ n_\mathrm{p}$	=	number of construction points
n_v	=	number of voxels
$\mathbf{u}(\mathbf{x})$	=	intensity velocity field, fluid velocity field
$u,\ v,\ w$	=	x-, y-, and z-components of $\mathbf{u}$
$\tilde{\mathbf{u}}(\tilde{\mathbf{x}})$	=	optical flow field
$\mathbf{x}$	=	spatial coordinate within reconstructed volume
$\tilde{\mathbf{x}}$	=	spatial coordinate within image plane
$\mathbf{y}^c$	=	the cth construction point, i.e. the location of the center of the cth $K(\cdot, \mathbf{y}^c)$
α^c	=	column matrix of weights for the cth $K(\cdot, \mathbf{y}^c)$ used in T-PFV estimation ($D \times 1$ column matrix)
α	=	aggregate column matrix of all α^c ($Dn_\mathrm{p} \times 1$ matrix)

*Graduate Student Research Assistant, Institute for Aerospace Studies, AIAA Student Member.
†Associate Professor, AIAA Senior Member, Current Address: School of Aerospace Engineering, Georgia Institute of Technology, adam.steinberg@gatech.edu
‡Assistant Professor, Institute for Aerospace Studies.

β = regularization parameter
γ^c = column matrix of weights for the cth $K(\cdot, \mathbf{y}^c)$ used in global approximation ($D \times 1$ column matrix)
γ = aggregate column matrix of all γ^c ($DN_\mathrm{p} \times 1$ matrix)
κ = wavenumber
λ_ν = inner length scale
σ = characteristic diameter of the Gaussian radial basis function/divergence-free basis function
$\phi(\mathbf{r})$ = radial basis function
Ω = reconstructed volume
$\Delta\Omega$ = volume per voxel
$|\cdot|$ = absolute value operator
∂ = partial derivative operator
$\hat{\cdot}$ = estimated either by tomographic particle image velocimetry or tomographic particle flow velocimetry
$\|\cdot\|$ = ℓ^2 norm
$\mathcal{F}\{\cdot\}$ = Fourier transform
$\otimes$ = row-wise multiplication

Subscripts/superscripts

CD = central difference discretization
df = divergence-free
DNS = Johns Hopkins University direct numerical simulation data
f = final tomogram
G = Gaussian
i = initial tomogram
PWS = piecewise constant with discontinuities across sub-domain boundaries
sd = sub-domain
TPFV = tomographic particle flow velocimetry
x, y, z = Cartesian directions

I. Introduction

Turbulent flows exhibit complex 3D motion with a large separation of scales. As such, the development of 3D whole-field velocimetry methods has greatly benefited the experimental study of turbulent flows. However, the development of whole-field velocimetry methods that readily resolve the inner length scales remains an active and important area of fluid mechanics research.

A. Tomographic Particle Image Velocimetry

The state-of-the-art in three-dimensional, three-component (3D3C) velocimetry is tomographic particle image velocimetry (T-PIV). With this method, a tracer-particle field is illuminated volumetrically and simultaneously imaged from multiple viewing angles, and the 3D Mie-scattering field is inferred from the simultaneous particle images via tomographic reconstruction. The resulting tomogram pairs are divided into interrogation boxes (IBs), and the average particle displacement is estimated via cross-correlation. In this way, T-PIV yields instantaneous 3D3C measurements of the fluid velocity field [1, 2].

T-PIV is a proven and robust technique that has been used to measure both instantaneous and time-resolved velocity fields of a wide variety of flows, including reacting flows [1–8]. Recently, Kazbekov et al. have even demonstrated that T-PIV is capable of resolving the inner length scales and providing measurements of the Reynolds averaged enstrophy transport budget in a premixed swirl flame for Karlovitz numbers between 11 and 45 [9].

Nevertheless, T-PIV has a number of shortcomings. In particular, there are three which stem from the cross-correlational nature of the technique.

1) **Spatial resolution**: Because cross-correlation yields one velocity estimate per IB, the spatial resolution of T-PIV is determined by the IB size [1, 10]. In practice, the minimum IB size is limited by three competing factors. Firstly, each IB must contain a sufficient number of particles such that the computed cross-correlation maps have readily identifiable peaks [10, 11]. Secondly, each particle must be imaged with an image diameter of at least two or three pixels so that the particle centroids can be located with sub-voxel precision, thereby preventing peak locking [10, 12]. Thirdly, the particle seeding density must be sufficiently low such that particle images do not

overlap. In practice, the optimal number of particles per IB is found to be on the order of ten, and the optimal IB length is found to be on the order of twenty voxels [9, 10]. Using state-of-the-art optics, Kazbekov et al. have been able to achieve a spatial resolution of approximately 250 μm [9].

2) **Accuracy**: The estimate for the average displacement provided by cross-correlation may differ significantly from the true average displacement, particularly when sub-IB displacement gradients are significant [10]. This error emerges because cross-correlation is essentially a particle-weighted spatial averaging operation, whereas the average displacement is uniformly weighted over the IB. In general, the spatial distribution of tracer particles is non-uniform.
3) **Consistency with the flow physics**: Cross-correlation does not incorporate knowledge of the physics of the measured flow. Indeed, strictly speaking, velocity fields measured by T-PIV do not satisfy physical laws. For example, the velocity field of a constant-density field as measured by T-PIV is piecewise constant and, hence, is not divergence-free. As such, the T-PIV estimate does not satisfy conservation of mass in this case. Consequently, missing or spurious velocity estimates typically can only be addressed by heuristic post-processing.

In this paper, we introduce a tomographic, particle-based velocimetry method that aims to address these shortcomings. Instead of inferring the velocity field via cross-correlation, this method, termed tomographic particle flow velocimetry (T-PFV), is based on a physics-constrained motion estimation framework which is inspired by optical flow estimation.

B. Brief Overview of Optical Flow Estimation

Optical flow estimation is a well-established computer vision framework [13–16]. In the past two decades, optical flow estimation has also found application in fluid velocimetry [17–26]. The goal of optical flow estimation is to determine the apparent motion of features in an image plane, that is, the optical flow field $\tilde{\mathbf{u}}$. Optical flow estimation is based on the premise that the planar image intensity field $\tilde{I}$ may be treated as a transported quantity.

In general, the exact transport of $\tilde{I}$ may be complex. However, it is often assumed that $\tilde{I}$ is conserved [13–16], that is to say

$$\tilde{I}(\tilde{\mathbf{x}} + \tilde{\mathbf{d}}, t + \Delta t) = \tilde{I}(\tilde{\mathbf{x}}, t). \tag{1}$$

Here $\tilde{\mathbf{x}}$ is the coordinate in the image plane, t is the time, and $\tilde{\mathbf{d}}$ is the optical flow displacement field over time interval Δt. Furthermore, it is often assumed that $\tilde{\mathbf{d}}$ is small, in which case Eq. 1 may be linearized as

$$\partial_t \tilde{I} + \nabla \tilde{I} \cdot \tilde{\mathbf{u}} = 0, \tag{2}$$

where $\partial_t \tilde{I}$ is the partial derivative of $\tilde{I}$ with respect to time, $\nabla \tilde{I}$ is the gradient of $\tilde{I}$, and $\tilde{\mathbf{u}} = \lim_{\Delta t,\ \|\tilde{\mathbf{d}}\| \to 0} \tilde{\mathbf{d}}/\Delta t$ is the optical flow field [13].

While it is simple, Eq. 2 only constrains the component of $\tilde{\mathbf{u}}$ that is normal to the level sets of $\tilde{I}$. This closure problem is a manisfestation of the well-known aperture problem [13, 14, 24]. While there are many schemes that have been developed to address the aperture problem, for fluid velocimetry purposes, regularized global variational schemes are most commonly used. Typically, such schemes seek the solutions to either

$$\min_{\tilde{\mathbf{u}}} \int_a \left\{ \left(\partial_t \tilde{I} + \nabla \tilde{I} \cdot \tilde{\mathbf{u}} \right)^2 + \beta_1 \|\nabla \tilde{\mathbf{u}}\|^2 \right\} \mathrm{d}a, \tag{3}$$

which is a scheme due to Horn and Schunck [13], or

$$\min_{\tilde{\mathbf{u}}} \int_a \left\{ \left(\partial_t \tilde{I} + \nabla \tilde{I} \cdot \tilde{\mathbf{u}} \right)^2 + \beta_2 \|\nabla (\nabla \cdot \tilde{\mathbf{u}})\|^2 + \beta_3 \|\nabla (\nabla \times \tilde{\mathbf{u}})\|^2 \right\} \mathrm{d}a, \tag{4}$$

which is a similar scheme due to Suter [15]. Here, $\beta_1, \beta_2, \beta_3$ are user-set regularization parameters, $\|\cdot\|$ denotes the ℓ^2 norm, and a denotes the image plane. Both of these schemes enforce smoothness of $\tilde{\mathbf{u}}$. The Horn-Schunck scheme does so by penalizing the gradient of $\tilde{\mathbf{u}}$, while the Suter scheme does so by penalizing the gradients of the divergence and curl of $\tilde{\mathbf{u}}$.

II. Description of Tomographic Particle Flow Velocimetry

A. Motion constraint equation

T-PFV is based on motion constraint equations that have the same form as those used in optical flow estimation. That is to say

$$I(\mathbf{x} + \mathbf{d}, t + \Delta t) = I(\mathbf{x}, t), \tag{5}$$

where I is the 3D tomographically reconstructed intensity field, and $\mathbf{d}$ is the intensity field displacement over time interval Δt. In the present formulation, T-PFV is based on the linearized form of Eq. 5, i.e.

$$\partial_t I + \nabla I \cdot \mathbf{u} = 0, \tag{6}$$

where $\mathbf{u} = \lim_{\Delta t,\ \|\mathbf{d}\|\to 0} \mathbf{d}/\Delta t$ is the intensity velocity field. Given an ideal tomographic reconstruction, in the limit of vanishing Stoke's drag, $\mathbf{u}$ tends to the fluid velocity field. As such, $\mathbf{u}$ may be interpreted as a direct estimate of the fluid velocity field.

While T-PFV is based on motion constraint equations with the same form as those used in optical flow estimation, there is a key difference between optical flow estimation and T-PFV. In optical flow estimation, the motion constraint equation relates the planar image intensity $\tilde{I}$ to the apparent motion of features in the image plane, i.e. the optical flow field $\tilde{\mathbf{u}}$. As such, optical flow estimation is inherently a 2D framework. In contrast, in T-PFV, the motion constraint equation relates the reconstructed 3D intensity field I to the 3D intensity velocity field $\mathbf{u}$. Hence, T-PFV is inherently a 3D method.

B. Aperture problem and Closure

As with Eq. 2, Eq. 6 is subject to the aperture problem. In T-PFV, we address the aperture problem using a global variational scheme. That is, we seek the solution to

$$\min_{\mathbf{u}} \int_{\Omega} (\partial_t I + \nabla I \cdot \mathbf{u})^2 \, \mathrm{d}\Omega, \tag{7}$$

where Ω is the reconstructed volume. However, T-PFV does not use a *regularized* global variational scheme. While the intensity velocity field of a tracer particle field should indeed be smooth, the regularization schemes listed above are rather heuristic and, hence, have the potential to over-smooth the estimated velocity field, especially in the case of highly turbulent flows. In T-PFV, closure of the motion estimation problem is instead achieved by applying physical constraints that are linear in $\mathbf{u}$. This is achieved by decomposing $\mathbf{u}$ as a linear combination of n_p physics-informed radial basis functions $K(\cdot, \mathbf{y}^c)$, viz.

$$\mathbf{u}(\mathbf{x}) = \sum_{c=1}^{n_\mathrm{p}} K(\mathbf{x}, \mathbf{y}^c)\alpha^c. \tag{8}$$

Here, $K(\cdot, \mathbf{y}^c),\ c = 1, \ldots, n_\mathrm{p}$ are 3×3 matrix-valued basis functions, which we leave undefined as of yet; $\mathbf{y}^c$ is the center of the cth basis function, here termed construction points; and $\alpha^c = [\alpha_x^c\ \alpha_y^c\ \alpha_z^c]^\top$ is a 3×1 column matrix of weights corresponding to the cth basis function, with each component corresponding to each spatial direction. Substituting Eq. 8 into the functional of Problem 7 and approximating the integral by the Riemann sum associated with the voxels of the reconstructed tomograms, the motion estimation problem may be recast as

$$\hat{\alpha} = \arg\min_{\alpha} \sum_{\ell=1}^{n_\mathrm{v}} \left[\partial_{t,\Delta t} I(\mathbf{x}^\ell) + \nabla_h I(\mathbf{x}^\ell) \cdot \sum_{c=1}^{n_\mathrm{p}} K(\mathbf{x}^\ell, \mathbf{y}^c)\alpha^c \right]^2 \Delta\Omega. \tag{9}$$

Here, $\partial_{t,\Delta t} I$ and $\nabla_h I$ are finite difference approximations to $\partial_t I$ and $\nabla_h I$, respectively, and $\mathbf{x}^\ell$ is the location of voxel ℓ. Consequently, the velocity estimation problem reduces to the problem of determining $\alpha^c = [\alpha_x^c\ \alpha_y^c\ \alpha_z^c]^\top\ \forall c$, given a judiciously chosen set of $K(\cdot, \mathbf{y}^c)$, each centered about a judiciously chosen distribution of n_p construction points $\mathbf{y}^c$.

C. Solution of Velocity Field Estimation Problem

Because the residual of the resulting minimization problem is linear in α^c, the motion estimation problem reduces to a standard linear least squares problem. The summation that appears within the brackets in Eq. 9 is simply

$$\mathbf{u}(\mathbf{x}^\ell) = \sum_{c=1}^{n_\mathrm{p}} K(\mathbf{x}^\ell, \mathbf{y}^c)\alpha^c. \tag{10}$$

Equation 10 can be evaluated at all voxel positions and rearranged into

$$\underbrace{\left(\begin{array}{c} u^1 \\ \vdots \\ \vdots \\ u^{n_\mathrm{v}} \\ \hline v^1 \\ \vdots \\ \vdots \\ v^{n_\mathrm{v}} \\ \hline w^1 \\ \vdots \\ \vdots \\ w^{n_\mathrm{v}} \end{array}\right)}_{3n_\mathrm{v}\times 1} = \underbrace{\left[\begin{array}{c|c|c} k_{xx} & k_{xy} & k_{xz} \\ \hline k_{yx} & k_{yy} & k_{yz} \\ \hline k_{zx} & k_{zy} & k_{zz} \end{array}\right]}_{3n_\mathrm{v}\times 3n_\mathrm{p}} \underbrace{\left(\begin{array}{c} \alpha_x^1 \\ \vdots \\ \alpha_x^{n_\mathrm{p}} \\ \hline \alpha_y^1 \\ \vdots \\ \alpha_y^{n_\mathrm{p}} \\ \hline \alpha_z^1 \\ \vdots \\ \alpha_z^{n_\mathrm{p}} \end{array}\right)}_{:=\,\alpha\ (3n_\mathrm{p}\times 1)}, \tag{11}$$

where k_{xx} etc. are $n_\mathrm{v} \times n_\mathrm{p}$ block matrices which are comprised of corresponding elements of $K(\mathbf{x}^\ell, \mathbf{y}^c)$ evaluated for corresponding values of ℓ and c. Provided that $n_\mathrm{v} \geq 3n_\mathrm{p}$*, Eq. 9 reduces to a linear least squares problem. That is,

$$\hat{\alpha} = \arg\min_{\alpha} \|b - A\alpha\|^2, \tag{12}$$

where

$$b = -\underbrace{\left(\begin{array}{c} \partial_{t,\Delta t} I(\mathbf{x}^1) \\ \vdots \\ \partial_{t,\Delta t}(\mathbf{x}^{n_\mathrm{v}}) \end{array}\right)}_{n_\mathrm{v}\times 1} \tag{13}$$

and

$$\begin{aligned} \underbrace{A}_{n_\mathrm{v}\times 3n_\mathrm{p}} = &\left(\begin{array}{c} \partial_{x,h} I(\mathbf{x}^1) \\ \vdots \\ \partial_{x,h} I(\mathbf{x}^{n_\mathrm{v}}) \end{array}\right) \otimes \left[\begin{array}{c|c|c} k_{xx} & k_{xy} & k_{xz} \end{array}\right] \\ &+ \left(\begin{array}{c} \partial_{y,h} I(\mathbf{x}^1) \\ \vdots \\ \partial_{y,h} I(\mathbf{x}^{n_\mathrm{v}}) \end{array}\right) \otimes \left[\begin{array}{c|c|c} k_{yx} & k_{yy} & k_{yz} \end{array}\right], \\ &+ \left(\begin{array}{c} \partial_{z,h} I(\mathbf{x}^1) \\ \vdots \\ \partial_{z,h} I(\mathbf{x}^{n_\mathrm{v}}) \end{array}\right) \otimes \left[\begin{array}{c|c|c} k_{zx} & k_{zy} & k_{zz} \end{array}\right] \end{aligned} \tag{14}$$

where $\otimes$ denotes row-wise multiplication. Once the weights $\hat{\alpha}^c$ have been found, the estimated velocity field is readily computed using

$$\hat{\mathbf{u}}_{\mathrm{TPFV}}(\mathbf{x}) = \sum_{c=1}^{n_\mathrm{p}} K(\mathbf{x}, \mathbf{y}^c)\hat{\alpha}^c. \tag{15}$$

*In practice, we find that n_p is less than, but on the order of, the number of particles, while n_v is much greater than the number of particles.

	T-PIV	T-PFV
Approximation space	Piecewise constant functions	Piecewise smooth, physics-informed functions
Projection method	Cross-correlation	Inspired by optical flow estimation

Table 1 Comparison of T-PIV and T-PFV in the language of numerical analysis.

D. Divergence-free Radial Basis Functions

At present, T-PFV has been formulated for constant-density flows, for which conservation of mass stipulates that

$$\nabla \cdot \mathbf{u} \equiv 0, \tag{16}$$

which is a linear constraint in $\mathbf{u}$. In this case, T-PFV aims to solve Problem 9 subject to Eq. 16. This is similar to the study of Ruhnau et al. [22], in which Problem 3 is solved subject to the time-independent equations governing Stokes flow. However, in applying the Stokes flow constraint, their formulation invokes yet another regularization scheme. A distinguishing characteristic of T-PFV is that the divergence-free constraint is applied in a way that avoids the use of regularization schemes entirely.

There exists a class of matrix-valued radial basis functions whose linear combination is a divergence-free vector field [27]. These divergence-free radial basis functions (RBF) may be derived from a given scalar RBF, as described in [28, 29]. In T-PFV, the divergence-free constraint can be applied by simply projecting the unknown velocity field onto the space spanned by a prescribed set of divergence-free radial basis functions.

E. Comparison with T-PIV

At this point, it is useful to set out a conceptual comparison of T-PIV and T-PFV. Both T-PIV and T-PFV use particles as flow tracers and tomographic reconstruction of particle tomogram pairs. However, there are key differences between these methods. T-PIV (i) treats particles as discrete entities, (ii) seeks the velocity that maximizes the cross-correlation between IB pairs in a piece-wise constant manner, and (iii) does not incorporate knowledge of the flow physics. In contrast, T-PFV (i) treats the reconstructed intensity as a spatially continuous variable, and (ii) seeks the continuous velocity field that minimizes the discrepancy between the intensity fields of a given tomogram pair using (iii) a basis function representation that is informed by known flow physics.

A comparison of T-PIV and T-PFV in the language of numerical analysis is perhaps also illuminating. Firstly, T-PIV uses an approximation space of piecewise constant basis functions, whereas T-PFV uses a richer approximation space of smooth, physics-informed basis functions. Secondly, T-PIV uses a projection method based on cross-correlation, whereas T-PFV uses a projection method inspired by optical flow estimation. This comparison is summarized in Table 1.

III. Demonstration of T-PFV

A. Description of Demonstration

In the remainder of this paper, we discuss a demonstration of T-PFV. This demonstration consists of estimating a section of the velocity field corresponding to the forced-isotropic DNS data available on the Johns Hopkins Turbulence Databases (JHTDB) [30, 31]. Specifically, a $256 \times 256 \times 128$ vx section of the DNS velocity field is estimated via T-PFV and an idealized implementation of T-PIV, and the results are compared.

The T-PFV estimate is computed from noise-free tomograms that are synthesized by (i) convecting particles within the DNS velocity field according to a four-stage explicit Runge-Kutta scheme coupled with piecewise cubic interpolation of the DNS velocity field, and (ii) smoothing the particle fields into $256 \times 256 \times 128$ vx intensity fields with a particle diameter of 16 vx. The tomograms contain 27 particles within each volume of $32 \times 32 \times 32$ vx, and the initial particle distribution is uniform. In addition, the temporal derivative of I is approximated by

$$\partial_{t,\Delta t} I(\mathbf{x}^\ell) = \frac{I_\mathrm{f}(\mathbf{x}^\ell) - I_\mathrm{i}(\mathbf{x}^\ell)}{\Delta t_\mathrm{fi}}, \tag{17}$$

and the gradient is approximated by

$$\nabla_h I(\mathbf{x}^\ell) = \frac{1}{2}\left[\nabla^\mathrm{CD} I_\mathrm{i}(\mathbf{x}^\ell) + \nabla^\mathrm{CD} I_\mathrm{f}(\mathbf{x}^\ell)\right]. \tag{18}$$

Here, I_f and I_i are the intensity fields corresponding to the final and initial tomograms, respectively; Δt_fi is the time interval between the final and initial tomograms; and ∇^CD denotes that the gradients are approximated according to a second-order central difference scheme.

The idealized T-PIV estimate is calculated by simply computing the average of the DNS field over IBs with a volume of $32 \times 32 \times 32$ vx. We note that the particular value of the IB size is not important here; an IB length of 32 vx is chosen simply because it is typical in T-PIV. Rather, it is the number of particles per IB that is important. In this demonstration, there are 27 particles per IB, which allows for a well-conditioned cross-correlation calculation over each IB. It is worth noting that 27 particles per IB is at or above the maximum of what is possible using tomographic reconstruction methods.

Finally, the T-PFV estimate is calculated using

$$K_{\mathrm{df,\,G}}(\mathbf{x}, \mathbf{y}^c; \sigma) = \frac{1}{\sigma^2} \exp\left(\frac{-\|\mathbf{x} - \mathbf{y}^c\|^2}{2\sigma^2}\right) \left[\frac{1}{\sigma^2}(\mathbf{x} - \mathbf{y}^c)(\mathbf{x} - \mathbf{y}^c)^\top + \left(D - 1 - \frac{\|\mathbf{x} - \mathbf{y}^c\|^2}{\sigma^2}\right) \mathcal{I}_D\right], \tag{19}$$

which is a divergence-free RBF derived from the Gaussian scalar RBF [29]

$$\phi(\mathbf{r}) = \phi_\mathrm{G}(\mathbf{r}; \sigma) = \exp(-\|\mathbf{r}\|^2 / 2\sigma^2). \tag{20}$$

Here, D is the number of spatial dimensions (3 in this case), and $\mathcal{I}_D$ is the $D \times D$ identity matrix. Furthermore, σ is a characteristic diameter of the RBF; it is a *hyperparamter*, which may be tuned. A value of σ equal to the IB length was found to be optimal in this demonstration case. These basis functions are distributed uniformly. It was found that for every 27 particles, the optimal number of basis functions was 8.

B. Domain Partitioning and Global Approximation in T-PFV Computation

Due to memory limitations, it was necessary to compute the T-PFV estimate piecewise over sub-domains of the volume considered. As such, the resulting estimated field $\hat{\mathbf{u}}_{\mathrm{TPFV,\,PWS}}$ was piecewise smooth and discontinuous across sub-domain boundaries. The $256 \times 256 \times 128$ vx volume was partitioned into sub-domains with a volume of $32 \times 32 \times 32$ vx, which contained 27 particles and corresponded to the IB size used in the idealized T-PIV estimation. Consequently, the velocity field was estimated piecewise over a total of $N_\mathrm{sd} = 256$ sub-domains, with $n_{\mathrm{p,\,sd}} = 8$ construction points per sub-domain.

The discontinuities between sub-domains were removed by globally approximating the piecewise-smooth field using the same Gaussian divergence-free RBFs used to perform the local T-PFV estimations. That is, the solution to

$$\hat{\gamma} = \arg\min_{\gamma} \int_\Omega \|\hat{\mathbf{u}}_{\mathrm{TPFV,\,PWS}}(\mathbf{x}) - \sum_{c=1}^{N_\mathrm{p}} K_{\mathrm{df,\,G}}(\mathbf{x}, \mathbf{y}^c)\gamma^c\|^2 \mathrm{d}\Omega \tag{21}$$

was computed, from which the globally smooth T-PFV estimate was computed by

$$\hat{\mathbf{u}}_{\mathrm{TPFV}}(\mathbf{x}) = \sum_{c=1}^{N_\mathrm{p}} K_{\mathrm{df,\,G}}(\mathbf{x}, \mathbf{y}^c)\hat{\gamma}^c. \tag{22}$$

Here N_p denotes the total number of construction points over all sub-domains used in the global approximation.

In a manner similar to the T-PFV estimation problem, Problem 21 reduces to a linear least squares problem when the integral is discretized. In this demonstration, the integral was approximated as a Riemann sum over a set of regularly distributed points that were sub-sampled at a rate of one sample point for every 4 voxels in each direction.

In addition, the value of σ used in the global approximation was equal to that used in the local T-PFV estimations. Furthermore, the distribution of construction points used for the global approximation was the same as that used for the T-PFV estimation. Hence, $N_\mathrm{p} = N_\mathrm{sd} \times n_{\mathrm{p,\,sd}} = 256 \times 8 = 2048$.

C. Results

Figure 1 shows the magnitude of the velocity field plotted over the slice which cuts through the center of the volume considered. Figures 1a, 1b, and 1c correspond to the idealized T-PIV estimate, DNS field, and T-PFV estimate,

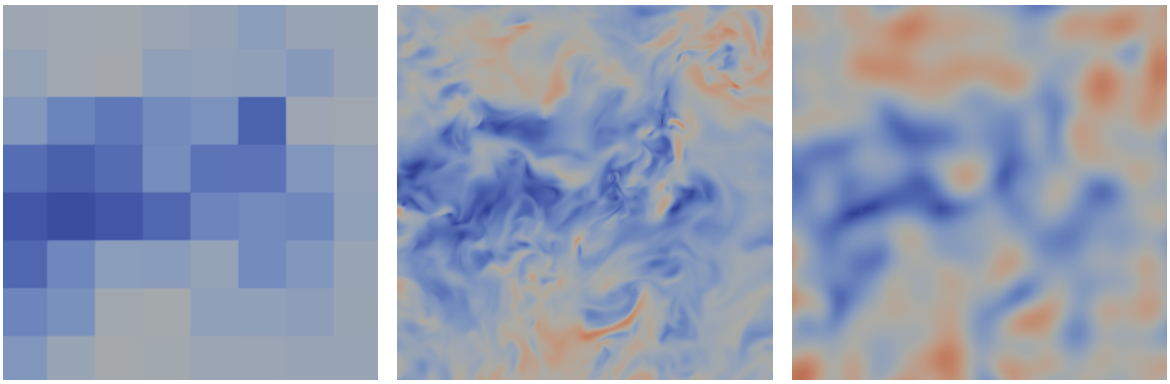

(a) Idealized T-PIV estimate. **(b) DNS.** **(c) T-PFV estimate.**

Fig. 1 Contour plot of magnitude of velocity over slice through center of volume. Slice is 256×256 vx wide.

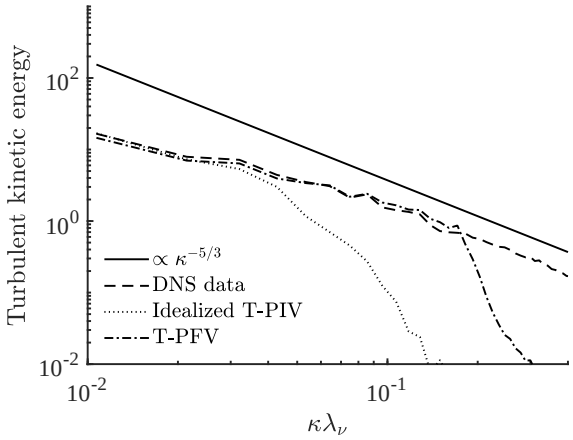

Fig. 2 Turbulent kinetic energy spectra of DNS field, idealized T-PIV estimate, and T-PFV estimate; $\kappa\lambda_\nu$ is the wavenumber non-dimensionalized by the inner length scale.

respectively. The T-PFV estimate is noticeably more resolved than the T-PIV estimate. Furthermore, the error relative to the DNS, defined as

$$e = \frac{\left(\int_\Omega \|\hat{\mathbf{u}} - \mathbf{u}_{\mathrm{DNS}}\|^2 \mathrm{d}\Omega\right)^{1/2}}{\left(\int_\Omega \|\mathbf{u}_{\mathrm{DNS}}\|^2 \mathrm{d}\Omega\right)^{1/2}}, \tag{23}$$

is 45% for the idealized T-PIV estimate and 33% for the T-PFV estimate[†].

Figure 2 shows the tubulent kinetic energy (TKE) spectra for the DNS field, idealized T-PIV estimate, and T-PFV estimate. The TKE of the T-PIV estimate was computed after smoothing the T-PIV velocity field via piecewise cubic interpolation. It is readily seen that T-PFV faithfully captures the TKE spectrum of the DNS field to significantly higher wavenumbers than idealized T-PIV.

Finally, Fig. 3 shows the spectrum of the error normalized by the spectrum of the DNS field, that is, $(|\mathcal{F}\{\hat{u} - u_{\mathrm{DNS}}\}|^2 + |\mathcal{F}\{\hat{v} - v_{\mathrm{DNS}}\}|^2 + |\mathcal{F}\{\hat{w} - w_{\mathrm{DNS}}\}|^2)/(|\mathcal{F}\{u_{\mathrm{DNS}}\}|^2 + |\mathcal{F}\{v_{\mathrm{DNS}}\}|^2 + |\mathcal{F}\{w_{\mathrm{DNS}}\}|^2)$ as a function of $\kappa\lambda_\nu$. Here, $\mathcal{F}$ denotes the Fourier transform, and $\kappa\lambda_\nu$ is the wavenumber non-dimensionalized by the inner length scale. For the sake of argument, if a normalized error threshold of 60% is chosen, the corresponding wavenumber for the T-PFV estimate is found to be approximately twice that of the idealized T-PIV estimate. That is, in this demonstration case, the spatial resolution of T-PFV is approximately twice that of idealized T-PIV.

[†]The integrals were approximated as voxel-wise Riemann sums.

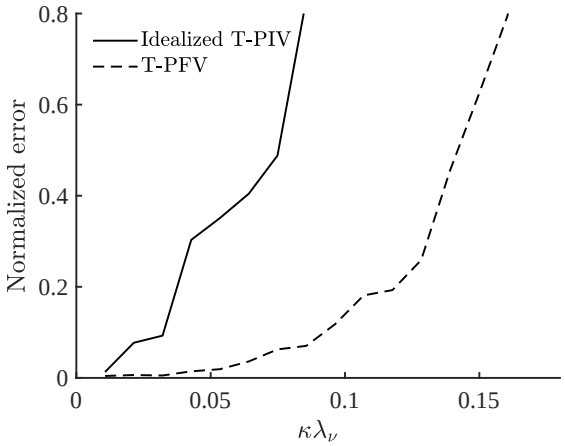

Fig. 3 Spectrum of the error normalized by the spectrum of the DNS field; $\kappa\lambda_\nu$ is the wavenumber non-dimensionalized by the inner length scale

D. Discussion

In particle-based velocimetry, for a given seeding density of tracer particles, any increase in spatial resolution is ultimately due to more efficient use of the available Mie-scattering data. In this demonstration, it was found that, using T-PFV, one divergence-free RBF could be placed for approximately every 3 particles. In contrast, cross-correlation would require $O(10)$ particles for each piecewise constant basis function. Consequently, this demonstration suggests that T-PFV allows the positioning of one order of magnitude more basis functions per unit volume than T-PIV, or, equivalently, approximately twice as many basis functions in each direction. Indeed, this corresponds to the observed twofold improvement in spatial resolution relative to T-PIV.

As for accuracy, the value of the relative error for T-PFV was found to be 12% lower than that for idealized T-PIV. This increase in accuracy follows from the improvement in spatial resolution.

IV. Conclusion and Future Work

In this paper, we present a first formulation of tomographic particle flow velocimetry (T-PFV), which is a 3D3C, particle-based velocimetry method that is based on a motion estimation framework inspired by optical flow estimation. However, unlike optical flow estimation, which is inherently 2D, T-PFV is an inherently 3D method. Furthermore, whereas optical flow estimation as applied to fluid velocimetry generally uses variational regularization schemes to address the aperture problem, T-PFV incorporates known flow physics to achieve closure. At present, T-PFV is formulated for constant-density flows.

In addition, we present a demonstration of the current formulation of T-PFV. The results suggest that T-PFV affords a twofold improvement in spatial resolution and a 12% decrease in the relative error as compared to T-PIV.

Future work will be focused on improving the efficiency and robustness of T-PFV. One avenue of future work is to modify the formulation from that based on divergence-free RBFs to one based on divergence-free polynomials. As noted above, the optimum number of RBFs is determined by the number of particles within a given volume, which in turn is determined by the limits of tomographic reconstruction methods. The comparatively local support of RBFs may be limiting the efficient use of available Mie-scattering data. Indeed, we found that the RBF diameter had to be set to relatively large values in order to achieve acceptable estimates. In contrast, divergence-free polynomials have comparatively global support and, thus, may be more suitable to T-PFV. In addition, divergence-free polynomials are known to achieve spectral convergence for sufficiently smooth flows [32]. While the use of divergence-free polynomials instead of divergence-free RBF would modify the formulation detailed in this paper slightly, our intention is to develop T-PFV as a framework rather than a particular scheme.

Going forward, the main challenge is to improve the robustness of T-PFV with respect to noise and, moreover, ghost particles. Currently, T-PFV is based on a differential motion constraint equation (Eq. 6). However, a differential formulation may not be robust against noise and ghost particles. As such, we are looking into generalizing to an integral formulation.

V. Acknowledgments

This work was supported by the US Air Force Office of Scientific Research under Grant FA9550-17 (Project Monitor Dr. Chiping Li) and the National Science and Engineering Research Council of Canada through an Alexander Graham Bell Canada Graduate Scholarship.

References

[1] Elsinga, G. E., Scarano, F., Wieneke, B., and van Oudheusden, B. W., "Tomographic particle image velocimetry," *Experiments in Fluids*, Vol. 41, No. 6, 2006, pp. 933–947.

[2] Scarano, F., "Tomographic PIV: principles and practice," *Measurement Science and Technology*, Vol. 24, No. 1, 2012, p. 012001.

[3] Coriton, B., Steinberg, A. M., and Frank, J. H., "High-speed tomographic PIV and OH PLIF measurements in turbulent reactive flows," *Experiments in fluids*, Vol. 55, No. 6, 2014, p. 1743.

[4] Coriton, B., and Frank, J. H., "High-speed tomographic PIV measurements of strain rate intermittency and clustering in turbulent partially-premixed jet flames," *Proceedings of the Combustion Institute*, Vol. 35, No. 2, 2015, pp. 1243–1250.

[5] Coriton, B., and Frank, J. H., "Experimental study of vorticity-strain rate interaction in turbulent partially premixed jet flames using tomographic particle image velocimetry," *Physics of Fluids*, Vol. 28, No. 2, 2016, p. 025109.

[6] Steinberg, A. M., Coriton, B., and Frank, J., "Influence of combustion on principal strain-rate transport in turbulent premixed flames," *Proceedings of the Combustion Institute*, Vol. 35, No. 2, 2015, pp. 1287–1294.

[7] Osborne, J. R., Ramji, S. A., Carter, C. D., Peltier, S., Hammack, S., Lee, T., and Steinberg, A. M., "Simultaneous 10 kHz TPIV, OH PLIF, and CH_2O PLIF measurements of turbulent flame structure and dynamics," *Experiments in Fluids*, Vol. 57, No. 5, 2016, p. 65.

[8] Osborne, J. R., Ramji, S. A., Carter, C. D., and Steinberg, A. M., "Relationship between local reaction rate and flame structure in turbulent premixed flames from simultaneous 10 kHz TPIV, OH PLIF, and CH_2O PLIF," *Proceedings of the Combustion Institute*, Vol. 36, No. 2, 2017, pp. 1835–1841.

[9] Kazbekov, A., and Steinberg, A. M., "Reynolds averaged enstrophy transport budgets measured in premixed swirl flames using μ-TPIV," *2018 Joint Propulsion Conference*, 2018, p. 4470.

[10] Raffel, M., Willert, C. E., Wereley, S. T., and Kompenhans, J., *Particle image velocimetry: a practical guide*, Springer, 2013.

[11] Keane, R. D., and Adrian, R. J., "Theory of cross-correlation analysis of PIV images," *Applied scientific research*, Vol. 49, No. 3, 1992, pp. 191–215.

[12] Prasad, A., Adrian, R., Landreth, C., and Offutt, P., "Effect of resolution on the speed and accuracy of particle image velocimetry interrogation," *Experiments in Fluids*, Vol. 13, No. 2, 1992, pp. 105–116.

[13] Horn, B. K., and Schunck, B. G., "Determining optical flow," *Artificial Intelligence*, Vol. 17, No. 1-3, 1981, pp. 185–203.

[14] Lucas, B. D., and Kanade, T., "An iterative image registration technique with an application to stereo vision," *Seventh International Joint Conference on Artificial Intelligence*, 1981, pp. 674–679.

[15] Suter, D., "Motion estimation and vector splines," *Proceedings of IEEE Conference on Computer Vision and Pattern Recognition*, Vol. 94, 1994, pp. 939–942.

[16] Fleet, D., and Weiss, Y., "Optical flow estimation," *Handbook of mathematical models in computer vision*, Springer, 2006, pp. 237–257.

[17] Quénot, G. M., Pakleza, J., and Kowalewski, T. A., "Particle image velocimetry with optical flow," *Experiments in Fluids*, Vol. 25, No. 3, 1998, pp. 177–189.

[18] Corpetti, T., Mémin, E., Santa-Cruz, A., Heitz, D., and Arroyo, G., "Optical flow estimation in experimental fluid mechanics," *Signal Processing and Its Applications, 2003. Proceedings. Seventh International Symposium on*, Vol. 1, IEEE, 2003, pp. 633–636.

[19] Corpetti, T., Heitz, D., Arroyo, G., Memin, E., and Santa-Cruz, A., "Fluid experimental flow estimation based on an optical-flow scheme," *Experiments in Fluids*, Vol. 40, No. 1, 2006, pp. 80–97.

[20] Ruhnau, P., Kohlberger, T., Schnörr, C., and Nobach, H., "Variational optical flow estimation for particle image velocimetry," *Experiments in Fluids*, Vol. 38, No. 1, 2005, pp. 21–32.

[21] Ruhnau, P., Yuan, J., and Schnörr, C., "On variational methods for fluid flow estimation," *Complex Motion*, Springer, 2007, pp. 124–145.

[22] Ruhnau, P., and Schnörr, C., "Optical stokes flow estimation: an imaging-based control approach," *Experiments in Fluids*, Vol. 42, No. 1, 2007, pp. 61–78.

[23] Yuan, J., Schnörr, C., and Mémin, E., "Discrete orthogonal decomposition and variational fluid flow estimation," *Journal of Mathematical Imaging and Vision*, Vol. 28, No. 1, 2007, pp. 67–80.

[24] Heitz, D., Mémin, E., and Schnörr, C., "Variational fluid flow measurements from image sequences: synopsis and perspectives," *Experiments in Fluids*, Vol. 48, No. 3, 2010, pp. 369–393.

[25] Liu, T., Merat, A., Makhmalbaf, M., Fajardo, C., and Merati, P., "Comparison between optical flow and cross-correlation methods for extraction of velocity fields from particle images," *Experiments in Fluids*, Vol. 56, No. 8, 2015, p. 166.

[26] Zhong, Q., Yang, H., and Yin, Z., "An optical flow algorithm based on gradient constancy assumption for PIV image processing," *Measurement Science and Technology*, Vol. 28, No. 5, 2017, p. 055208.

[27] Narcowich, F. J., and Ward, J. D., "Generalized Hermite interpolation via matrix-valued conditionally positive definite functions," *Mathematics of Computation*, Vol. 63, No. 208, 1994, pp. 661–687.

[28] Lowitzsch, S., "Approximation and interpolation employing divergence-free radial basis functions with applications," Ph.D. thesis, Texas A&M University, 2004.

[29] Macêdo, I., and Castro, R., "Learning divergence-free and curl-free vector fields with matrix-valued kernels," *Instituto Nacional de Matematica Pura e Aplicada, Brasil, Tech. Rep*, 2008.

[30] Perlman, E., Burns, R., Li, Y., and Meneveau, C., "Data exploration of turbulence simulations using a database cluster," *Proceedings of the 2007 ACM/IEEE Conference on Supercomputing*, ACM, 2007, p. 23.

[31] Li, Y., Perlman, E., Wan, M., Yang, Y., Meneveau, C., Burns, R., Chen, S., Szalay, A., and Eyink, G., "A public database cluster and applications to study Lagrangian evolution of velocity increments in turbulence," *Journal of Turbulence*, Vol. 9, No. 31, 2008.

[32] Sacchi Landriani, G., and Vandeven, H., "Polynomial approximation of divergence-free functions," *Mathematics of Computation*, Vol. 52, No. 185, 1989, pp. 103–130.